

# Tracing Like a Clinician: Anatomy-Guided Spatial Priors for Cephalometric Landmark Detection

Sidhartha Mohapatra<sup>1</sup> Dr. Pallavi Mohanty, DDS<sup>2</sup>

<sup>1</sup>Founder & CTO, CephTrace <sup>2</sup>Clinical Advisor, CephTrace

sidhartha@cephtrace.com

## Abstract

When orthodontists trace cephalometric radiographs, they follow a structured workflow: identify the soft tissue profile, partition the skull into anatomical regions, trace contours, and locate landmarks using geometric definitions—yet no automated system replicates this reasoning. We present a five-phase anatomy-guided initialization pipeline that translates this clinical workflow into computational operations, producing confidence-weighted spatial attention priors for a downstream HRNet-W32 detector. On 1,502 radiographs from three sources spanning 7+ imaging devices, the system achieves 1.04 mm mean radial error on 25 landmarks—surpassing prior state-of-the-art (1.23 mm on 19 landmarks) by 15.4%, with twelve landmarks below 1 mm. A three-way controlled ablation reveals two striking findings. First, removing anatomical priors does not merely slow convergence—it destroys generalization: both models converge to  $\sim 1.03$  mm on validation, but diverge to 1.94 vs. 1.04 mm on the test set. Second, replacing anatomical priors with *random-position* Gaussians produces even worse generalization (2.24 mm), confirming that the improvement derives from anatomically correct positioning, not additional input channels. Clinical domain knowledge encoded as spatial priors provides an inductive bias that architecture and data augmentation alone do not provide.

## 1 Introduction

Cephalometric analysis—the quantitative assessment of craniofacial morphology from lateral skull radiographs—underpins orthodontic diagnosis for millions of patients annually [1]. Precise identification of anatomical landmarks enables measurements that classify skeletal relationships, guide treatment, and track growth. Manual identification requires 15–20 minutes per radiograph and exhibits observer variability of  $\sim 0.9$ – $1.4$  mm [2], creating both a quality bottleneck and a compelling automation opportunity.

Deep learning has driven steady progress, from random forest regression-voting [3] through cascaded CNNs [4] to multi-head residual networks achieving 1.23 mm on 19 landmarks [6]. Yet a fundamental pattern persists: **all published systems treat landmark detection as direct regression from raw pixels**, without structured anatomical guidance.

This produces predictable failures. Landmarks in low-contrast regions (PNS), ambiguous concavities (B-point at 5.70 mm in our baseline), and structures requiring wide context (Gonion) consistently exceed the 2 mm clinical threshold. These failures are surprising because clinicians do not struggle with these landmarks. An orthodontist follows a structured workflow [1]: (1) identify the soft tissue profile, (2) partition structures into regions, (3) trace bony contours, (4) locate landmarks using geometric definitions, and (5) derive remaining landmarks from known relationships.

### Contributions.

1. **Clinically-defined zone decomposition:** five anatomical zones with region-specific enhancement, anchored to the detected soft tissue profile.
2. **Topology-based anchor extraction:** the first translation of textbook landmark definitions [1] into orientation-invariant computational geometry.
3. **Confidence-weighted attention priors:** three-tier Gaussian maps calibrated to anatomical ambiguity.
4. **A generalization finding:** a three-way ablation (no priors / random priors / anatomical priors) shows that only anatomically correct positioning improves generalization—random priors are worse than no priors.

## 2 Related Work

**The field has converged on direct heatmap regression.** Since the ISBI 2015 Challenge [2], progressively powerful architectures—random forests [3], cascaded CNNs [4], attentive feature pyramids [5], attention-guided regression [10], multi-head residual networks [6]—have driven MRE from 1.67 to 1.23 mm on 19 landmarks. The CL-Detection 2023 challenge [7] extended to 38 landmarks across 7 devices.

**Attempts to add anatomical context remain implicit.** Bayesian CNNs [8] model landmark uncertainty. Oh et al. [11] extract multi-scale context features. CEPHMark-Net [12] fuses semantic features in a two-stage framework. CephNet [9] uses dual attention for inter-landmark relationships. All learn context *implicitly*—none encodes the structured clinical workflow that gives human experts their advantage on difficult landmarks.

**The gap.** No published system uses clinically-defined zone decomposition, per-zone contrast optimization, adaptive contour simplification with clinically-motivated tolerances,

topology-based geometric extraction, or confidence-weighted spatial priors with per-landmark spread parameters.

### 3 Method

Our system comprises five sequential phases (Fig. 1), each mirroring a step in the clinical tracing workflow.

#### 3.1 Phase A: Soft Tissue Profile Detection

The pipeline begins with the soft tissue profile—the air-skin boundary, the highest-contrast feature in any lateral cephalogram regardless of exposure quality, patient age, or imaging device. A MobileNetV2+U-Net (~6.6M parameters) produces a binary mask at  $512 \times 512$ , trained with Dice+BCE loss on 1,000 radiographs, achieving test Dice of 0.80 (Fig. 2). Six soft tissue landmarks (Pronasale, Subnasale, Upper/Lower Lip, Soft Tissue Pogonion, Suprapogonion) are extracted geometrically from the mask contour in Phase B.

#### 3.2 Phase B: Adaptive Zone Partitioning

Using the profile as an anatomical anchor, the image is partitioned into five zones, each containing a clinically-related group of structures: (1) Cranial Base (Sella, Basion), (2) Mid-face (Nasion, Orbitale, ANS, PNS, A-point, upper incisors), (3) Mandible (Gonion, Menton, Gnathion, Pogonion, B-point, lower incisors), (4) Posterior (Porion, Condylion, Articulare), and (5) Soft Tissue (Pronasale, Subnasale, lips). Each zone receives region-specific CLAHE enhancement optimized for its dominant structures—aggressive enhancement for the small (~10 mm) pituitary fossa in Zone 1, minimal enhancement for the already-high-contrast soft tissue profile in Zone 5 (Fig. 3). Zone boundary calibration achieved 100% landmark containment across all 25 target landmarks on 1,502 images with zero failures.

#### 3.3 Phase C: Per-Zone Contour Segmentation

Four segmentation models (same MobileNetV2+U-Net architecture as Phase A, ~6.6M parameters each) detect bony contours within each zone in parallel: cranial base contour (Ba→S→N), palatal plane (PNS→ANS), mandibular border (Condylion through Gonion to the symphysis), mandibular symphysis subregion (B→Pog→Gn→Me), and the upper and lower incisor axes. Training data was generated by connecting annotated landmarks in clinically-defined anatomical order and thickening the resulting polylines into segmentation masks—a bootstrap approach that produces usable training data from existing landmark annotations without requiring separate contour annotation. A visibility masking system handles heterogeneous multi-source annotations where the three source datasets label different landmark subsets. Per-zone test Dice: 0.37–0.54.

Table 1: Anchor extraction: topology-based rules translating clinical definitions [1] into computational geometry.

Anchor	Contour	Rule
Sella	Ba→S→N	Max chord dev., 20–60% arc
Nasion	Ba→S→N	Last endpoint
ANS	PNS→ANS	Last endpoint
Menton	B→Pog→Gn→Me	Last endpoint
Pogonion	B→Pog→Gn→Me	Max chord dev., 10–65%
Gonion	Co→Ar→Go→...	Max curvature, 15–50%
Pronasale	Soft tissue	Phase A extraction

#### 3.4 Phase D: Adaptive Abstraction and Anchor Extraction

This phase—the primary methodological contribution—contains *zero trainable parameters*. All operations are deterministic geometric computations derived from clinical anatomy definitions.

**Adaptive Douglas-Peucker simplification.** Contour poly-lines are simplified using per-contour-class tolerances derived from clinical precision requirements: 0.5 mm for structures where subtle concavities define landmarks (mandibular symphysis, incisor axes), 1.0 mm for curvature-critical contours (mandibular border, palatal plane), and 2.0 mm for structures where only coarse shape matters (cranial vault). The key insight is that different anatomical structures require fundamentally different levels of geometric fidelity—a uniform tolerance either over-simplifies the symphysis or under-simplifies the vault.

**Topology-based anchor extraction.** Seven landmarks are extracted using orientation-independent geometric rules (Table 1). Unlike prior systems that assume a fixed patient orientation, our rules operate on contour topology—endpoint order, cumulative arc-length fractions, perpendicular chord deviation, and discrete curvature—making extraction invariant to orientation, resolution, and projection geometry (Fig. 4).

**Evaluation scope.** Table 3 reports accuracy on contours constructed from ground-truth landmark positions, validating that the geometric rules correctly identify landmarks on clean input. In production, contours come from Phase C models (Dice 0.37–0.54), introducing additional extraction error. The deployed system has operated with zero inference failures; a systematic production-path evaluation is ongoing work.

#### 3.5 Phase E: Attention Map Generation

An MLP (114,532 parameters;  $14 \rightarrow 256 \rightarrow 256 \rightarrow 128 \rightarrow 64 \rightarrow 36$ ) predicts 18 derived landmark positions from 7 normalized anchor coordinates, trained with masked L1 loss to handle heterogeneous annotations. The model encodes anatomical proportional relationships—e.g., Orbitale is inferior to Nasion on the orbital rim; A-point lies at the maxillary concavity between ANS and the upper incisor root—achieving 3.55 mm MRE with 95.9% SDR@8mm on 18 derived landmarks.

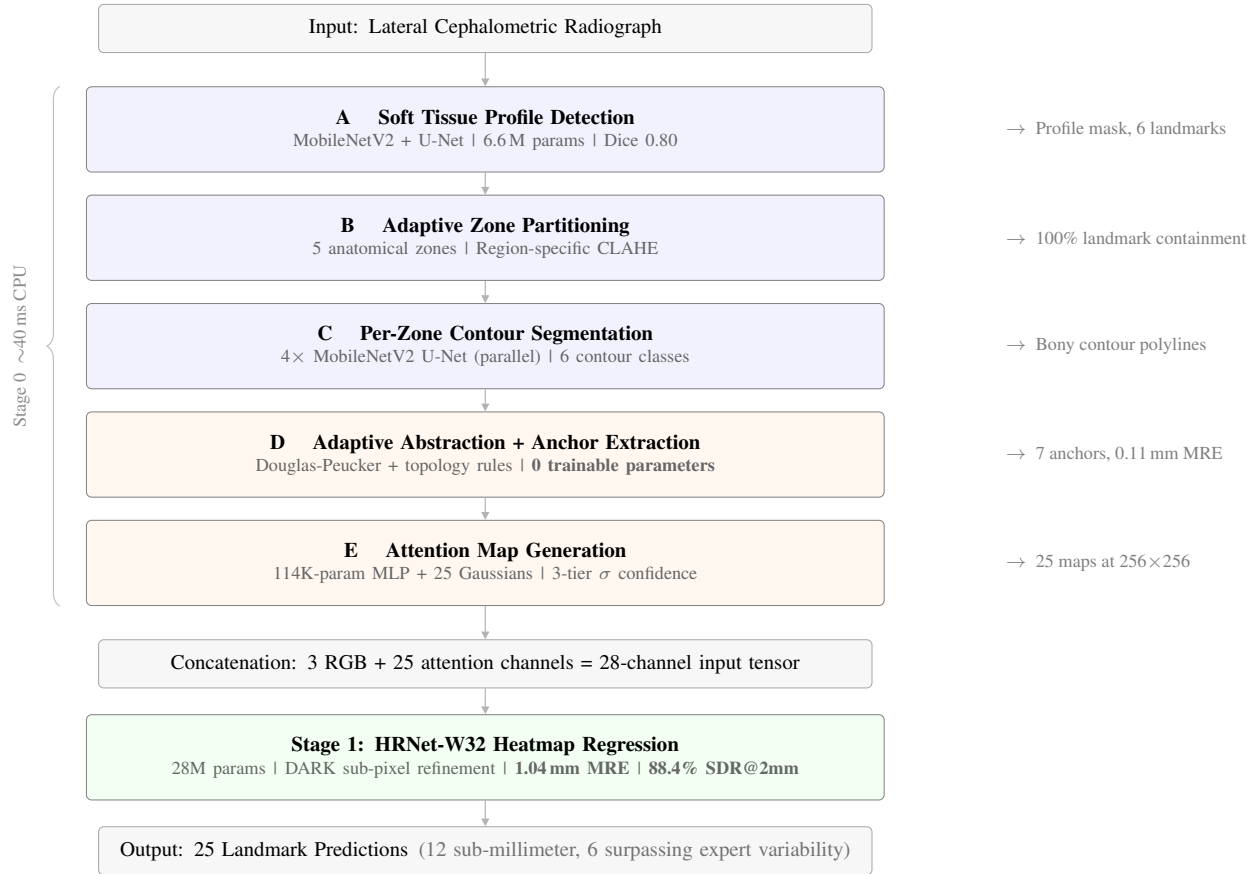


Figure 1: **System architecture.** Five phases progressively extract anatomical information. Phases A–C use learned segmentation; Phase D applies zero-parameter geometric rules from clinical definitions; Phase E generates confidence-weighted spatial priors. Total Stage 0:  $\sim 40$  ms on CPU.

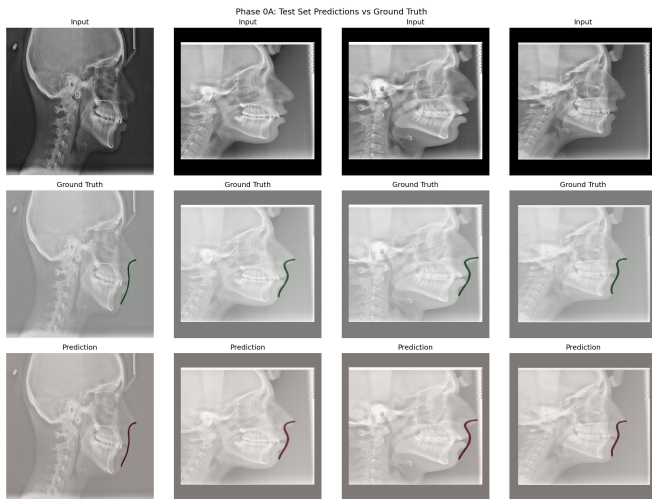


Figure 2: Phase A on four test cases spanning imaging devices. Top: inputs. Middle: ground-truth masks. Bottom: predictions. The model reliably detects the air-skin boundary from forehead through chin.

For each of 25 landmarks (7 anchors + 18 derived), a 2D Gaussian attention map  $A_k(x, y) = \exp\left(-\frac{(x-\hat{x}_k)^2 + (y-\hat{y}_k)^2}{2\sigma_k^2}\right)$

is generated, where  $\sigma_k$  encodes a three-tier confidence classification: high ( $\sigma=5-7$  px) for unambiguous anchors (Sella, Nasion, Menton, ANS, Pronasale), medium ( $\sigma=8-13$  px) for moderately ambiguous landmarks, and low ( $\sigma=18-22$  px) for the most difficult targets (Porion, PNS, B-point, Basion, Condylion). The 25 maps are concatenated with RGB to form a 28-channel input tensor for the downstream detector (Fig. 5).

## 4 Downstream Integration

**Stage 1.** HRNet-W32 ( $\sim 28$ M parameters) receives the 28-channel tensor with attention channels initialized at  $0.1 \times$  Kaiming scale. Training uses MSE loss with per-landmark visibility masking, fixed-sigma Gaussians by clinical tier (high=1.5 px, medium=2.5 px, low=4.0 px), AdamW ( $\text{lr}=3 \times 10^{-4}$ , weight decay 0.01), CosineAnnealingWarmRestarts scheduler, and DARK sub-pixel coordinate extraction. Horizontal flip is excluded as anatomically invalid for cephalograms.

**Stage 2.** A refinement network (ResNet-18 backbone with 25 independent MLP heads) extracts anatomically-adaptive patches around each Stage 1 prediction and learns per-landmark offset corrections. Seven priority landmarks (those



Figure 3: Phase B: Five anatomical zones with region-specific contrast enhancement. From left: cranial base (aggressive CLAHE for pituitary fossa), midface (bone-air sharpening), mandible (cervical spine suppression), posterior (ear canal enhancement), soft tissue (minimal, preserving high-contrast profile). Zone boundaries are adaptively anchored to the Phase A soft tissue profile.

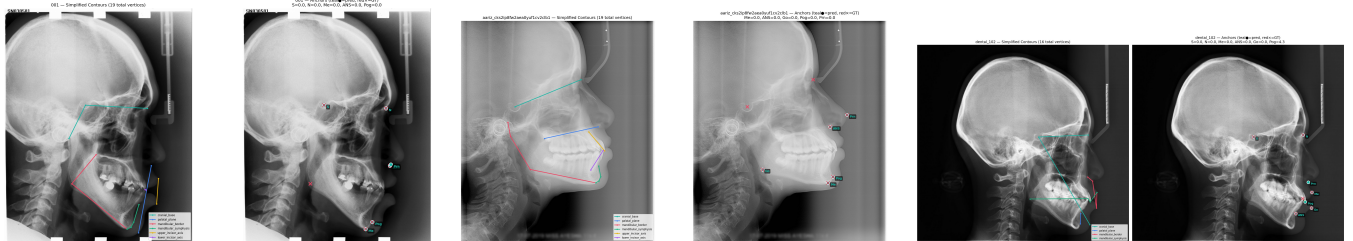


Figure 4: Phase D results on three datasets (ISBI, CEPHA29, DentalCepha). Left panels: simplified contours color-coded by anatomical class. Right panels: extracted anchors (teal circles) vs. ground truth (red crosses). Most anchor errors are 0.0 mm; Pogonion reaches 4.3 mm on the DentalCepha case (right) due to shallow symphysis curvature—the primary failure mode (see Section 5.6).

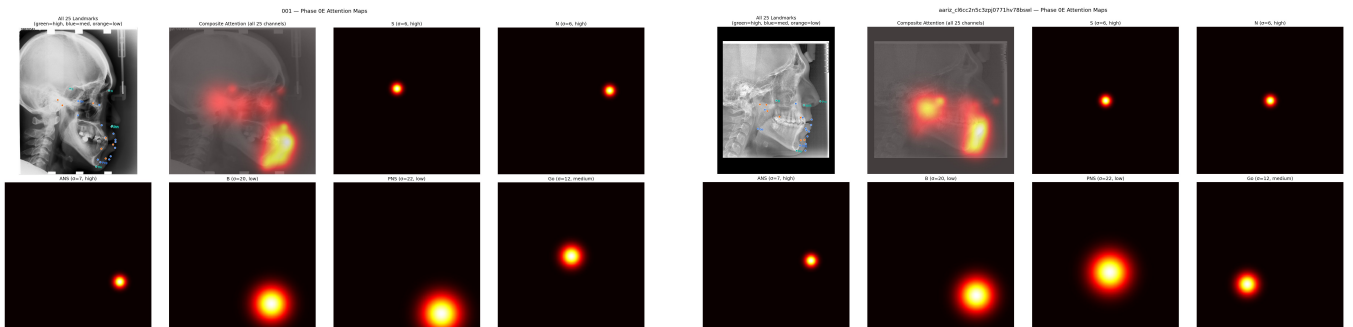


Figure 5: Phase E: Confidence-weighted attention maps on two cases (ISBI left, CEPHA29 right). Top-left: 25 predicted landmarks by confidence tier (green=high, blue=medium, orange=low). Top-right: composite attention overlay. Bottom row: individual channels for ANS ( $\sigma=7$ , tight), B-point ( $\sigma=20$ , broad), PNS ( $\sigma=22$ , broadest), Gonion ( $\sigma=12$ , medium)—demonstrating how the three-tier system calibrates spatial guidance to landmark ambiguity.

with  $\text{SDR}@2\text{mm} < 85\%$ ) received targeted specialist training. The remaining 18 heads are frozen, preserving Stage 1 accuracy exactly ( $\Delta=0.000$  mm by construction).

## 5 Experiments

### 5.1 Datasets

Three datasets were combined with a unified 25-landmark canonical set and cross-dataset name resolution (e.g., ISBI’s “U1”→“U1\_tip”, CEPHA29’s “Cd”→“Co”). Stratified split: 1,201/150/151 (train/val/test) by source (Table 2).

Table 2: Training data: 1,502 images from three sources.

Dataset	Images	Landmarks	Scanners
ISBI 2015 [2]	400	19	1
CEPHA29 [7, 13]	1,000	29	7
DentalCepha	102	19	Variable
<b>Combined</b>	<b>1,502</b>	<b>25</b>	<b>7+</b>

Table 3: Phase D: anchor extraction accuracy (ground-truth contours).

Anchor	N	MRE (mm)	SDR@2mm
Sella	502	0.00	100.0%
Nasion	502	0.00	100.0%
Menton	1,502	0.00	100.0%
ANS	1,502	0.00	100.0%
Gonion	878	0.07	99.4%
Pogonion	1,502	0.52	89.1%
Pronasale	1,000	0.00	100.0%
<b>Overall</b>	<b>7,388</b>	<b>0.11</b>	<b>97.7%</b>

Table 4: Three-way ablation. All three models converge to  $\sim 1.02$ – $1.03$  mm on validation; only anatomical priors maintain accuracy on the held-out test set.

Condition	Val MRE	Test MRE	Gap	SDR@2
No priors	$\sim 1.03$	1.938	+88%	87.1%
Random priors	$\sim 1.02$	2.240	+120%	81.7%
<b>Anatomical (Ours)</b>	$\sim 1.03$	<b>1.043</b>	<b>+1%</b>	<b>88.4%</b>

## 5.2 Stage 0 Performance

Phase E derived landmarks achieve 3.55 mm MRE (95.9% SDR@8mm) on 18 landmarks. Notably, B-point initialization at 3.45 mm already surpasses our baseline system’s final production error of 5.70 mm for this landmark. PNS initialization at 4.01 mm represents the first successful automated localization of this landmark (baseline:  $\sim 193$  mm, effectively random).

## 5.3 Ablation: Anatomy-Guided Priors

To isolate Stage 0’s contribution, we conducted two controlled ablations: (1) removing attention priors entirely (3-channel RGB input), and (2) replacing anatomical priors with *random-position* Gaussians (same  $\sigma$  tiers, random centers). All other variables were held constant: splits (seed=42), architecture, hyperparameters, augmentation, loss, and evaluation.

**Random priors are worse than no priors.** A model trained with random-position attention maps (same  $\sigma$  tiers, random centers, fully converged at epoch 46 with early stopping) achieved 2.24 mm test MRE—15% worse than no priors (1.94 mm) and  $2.15\times$  worse than anatomical priors (1.04 mm). Critically, all three models converge to nearly identical validation MRE ( $\sim 1.02$ – $1.03$  mm), confirming that the divergence is purely a *generalization* phenomenon. The validation-to-test gap forms a clear hierarchy: 1% for anatomical priors, 88% for no priors, and 120% for random priors (Table 4, Fig. 6). This confirms that the improvement from Stage 0 derives specifically from *anatomically correct positioning*: additional channels with incorrect spatial information do not merely fail to help—they actively degrade generalization by providing a misleading signal for the model to overfit to.

**Differential benefit pattern.** Comparing anatomical priors vs. no priors, soft tissue landmarks gained most (Pronasale +1.78 mm, Lower Lip +1.51 mm, Subnasale

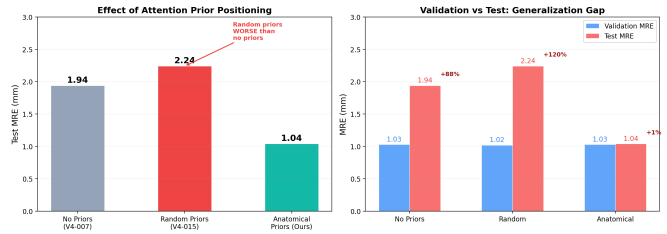


Figure 6: Three-way ablation. Left: test MRE across conditions. Right: the generalization gap (validation-to-test divergence) reveals that random priors produce the worst generalization (120% gap), while anatomical priors maintain near-perfect alignment (1% gap).

Table 5: Per-landmark results (held-out test set, sorted by MRE).

Landmark	MRE	SDR@2	N	Zone
Gnathion	0.48	97.4	151	Mand.
ANS	0.48	100.0	151	Mid.
Subnasale	0.54	98.2	111	Soft
Sella	0.56	99.3	151	Cran.
Menton	0.58	98.0	151	Mand.
Pogonion	0.58	96.0	151	Mand.
L1 tip	0.69	96.0	151	Mand.
Lower Lip	0.79	92.1	101	Soft
Pronasale	0.79	99.0	101	Soft
Upper Lip	0.84	94.1	101	Soft
U1 tip	0.89	89.4	151	Mid.
L1 root	0.95	88.7	141	Mand.
Soft Pog.	1.00	93.1	101	Soft
A-point	1.10	86.1	151	Mid.
U1 root	1.10	85.8	141	Mid.
Articulare	1.15	86.8	151	Post.
Gonion	1.19	82.8	151	Mand.
B-point	1.26	79.5	151	Mand.
Nasion	1.43	98.0	151	Cran.
Orbitale	1.52	74.2	151	Mid.
Condylion	1.56	76.6	111	Post.
Pm	1.63	77.5	40	Mand.
Porion	1.80	73.5	151	Post.
Basion	1.86	66.0	50	Cran.
PNS	2.06	67.5	151	Mid.
<b>Overall</b>	<b>1.04</b>	<b>88.4</b>	<b>3263</b>	—

+1.51 mm), followed by anatomically ambiguous bony landmarks (Condylion +1.04 mm, Pogonion +1.03 mm, Gonion +1.03 mm), with minimal impact on high-contrast bony landmarks (Articulare +0.31 mm). This gradient mirrors the clinical value of the workflow encoded by Stage 0.

**Statistical significance.** Bootstrap resampling ( $n=10,000$ ) confirms the mean MRE improvement of 0.880 mm has a 95% CI of [0.702, 1.050] mm ( $p < 0.0001$ ).

## 5.4 Full Pipeline Results

Six landmarks achieve sub-0.6 mm MRE—surpassing the  $\sim 0.9$ – $1.4$  mm observer variability reported for expert clinicians [2]. Twelve of 25 landmarks are sub-millimeter. The system detects all 25 landmarks, compared to 19 in most published systems (Table 5).

Table 6: Comparison with published methods. We include a 19-landmark subset for fair comparison with prior work.

System	LM	MRE	SDR@2	Data
Lindner [3]	19	1.67	75.0	ISBI
BCNN [8]	19	1.53	82.1	ISBI
AFPF [5]	19	1.17	86.7	ISBI (val)
CephRes-MHNet [6]	19	1.23	85.5	CEPHA29
<b>Ours (25 LM)</b>	<b>25</b>	<b>1.04</b>	<b>88.4</b>	Combined
<b>Ours (19 LM)</b>	<b>19</b>	<b>1.02</b>	<b>88.7</b>	Combined

## 5.5 State-of-the-Art Comparison

**Fair comparison note.** Direct comparison across studies is complicated by differences in datasets, splits, and landmark subsets. Our system trains on a more challenging multi-source dataset (7+ devices vs. single-source benchmarks) and detects 25 landmarks vs. the standard 19. On the common 19-landmark subset, our 1.02 mm MRE represents a 17.1% reduction from the best published result (1.23 mm). We consider multi-source training a stricter test of generalization than single-source evaluation.

## 5.6 Failure Analysis

**PNS (2.06 mm, 67.5% SDR@2mm).** The posterior nasal spine sits at a low-contrast palatal junction, receiving only a broad attention prior ( $\sigma=22$ ). Improvement requires better Phase C palatal plane segmentation. **Basion (1.86 mm, 66.0%).** Obscured by cervical vertebral overlap, with only 50 test samples (high metric variance). **Pogonion on Dental-Cepha (4.3 mm, Fig. 4 right).** Shallow symphysis curvature causes the chord deviation rule to select a displaced point—the primary failure mode for skeletal Class II deep-bite patients with minimal anterior chin prominence.

# 6 Discussion

## 6.1 Why Do Priors Improve Generalization?

The three-way ablation reveals a hierarchy of generalization behavior that illuminates the mechanism. All three models—no priors, random priors, anatomical priors—converge to  $\sim 1.02$ – $1.03$  mm on validation. They diverge only on the held-out test set: 1.94 mm without priors (88% gap), 2.24 mm with random priors (120% gap), and 1.04 mm with anatomical priors (1% gap).

Two aspects of this pattern are informative. First, the no-prior model’s 88% gap demonstrates that on a multi-source dataset spanning 7+ imaging devices, the network exploits device-specific texture patterns that correlate with landmark positions in the training distribution but do not transfer. Second, the random-prior model’s *larger* gap (120%) demonstrates that incorrect spatial information does not merely fail to regularize—it provides an additional misleading signal to overfit to. The model learns to trust the random channel positions during training, then those positions bear no anatomical

relationship to landmarks on unseen images, compounding the generalization failure.

Anatomical priors break this pattern because they are *device-independent*: computed from contour geometry rather than pixel intensity, they constrain the model’s search space to anatomically plausible regions regardless of scanner technology. This structured inductive bias is complementary to data augmentation—augmentation diversifies the input distribution, while anatomical priors constrain the hypothesis space. Together they enable the 1% generalization gap that makes clinical deployment viable.

## 6.2 Clinical Impact

At 1.04 mm, automated analysis falls within expert observer variability ( $\sim 0.9$ – $1.4$  mm) for the majority of measurements. The most consequential improvement is B-point ( $5.70 \rightarrow 1.26$  mm), which directly impacts the ANB skeletal classification metric. An error of 5.70 mm at B-point can shift ANB by 3–4 degrees—sufficient to misclassify a skeletal relationship and alter a treatment plan. At 1.26 mm, B-point contributes less than 1 degree to ANB variance, which is clinically insignificant. Clinical validation by Dr. Mohanty confirmed anatomically plausible placement across Class I, II, III, bimaxillary protrusion, and hyperdivergent cases.

## 6.3 Cross-Dataset Generalization

The system generalizes consistently across imaging devices (Fig. 8): CEPHA29 (1.23 mm, 7 scanners, 101 test images), ISBI (1.55 mm, single 2009-era Soredex scanner, 40 test images), and DentalCepha (0.74 mm, variable devices, 10 test images).<sup>1</sup> The higher ISBI error is expected—these are the oldest images in the dataset with the most film grain and lowest resolution. The strong DentalCepha performance despite having the fewest training samples (102 total) suggests the anatomy-guided priors provide effective regularization even in low-data regimes.

## 6.4 Broader Applicability

The zone decomposition principle is not specific to cephalometry. Any medical imaging domain where (a) landmarks are defined by geometric relationships to anatomical structures, (b) different structures require different image processing, and (c) structured clinical workflows exist for manual annotation could benefit from the same approach. Cardiac landmark detection (chamber segmentation as zones), musculoskeletal alignment (bone contour zones), and dental CBCT analysis (tooth-jaw segmentation) are immediate candidates. The topology-based geometric extraction rules (Section 3.4) generalize to any domain where landmarks are defined as curvature extrema, endpoints, or inflection points on anatomical contours.

<sup>1</sup>Per-source MRE computed from pre-extracted coordinates with approximate resolution normalization; absolute values differ slightly from heatmap-space evaluation in Table 5. Relative rankings across sources are robust.

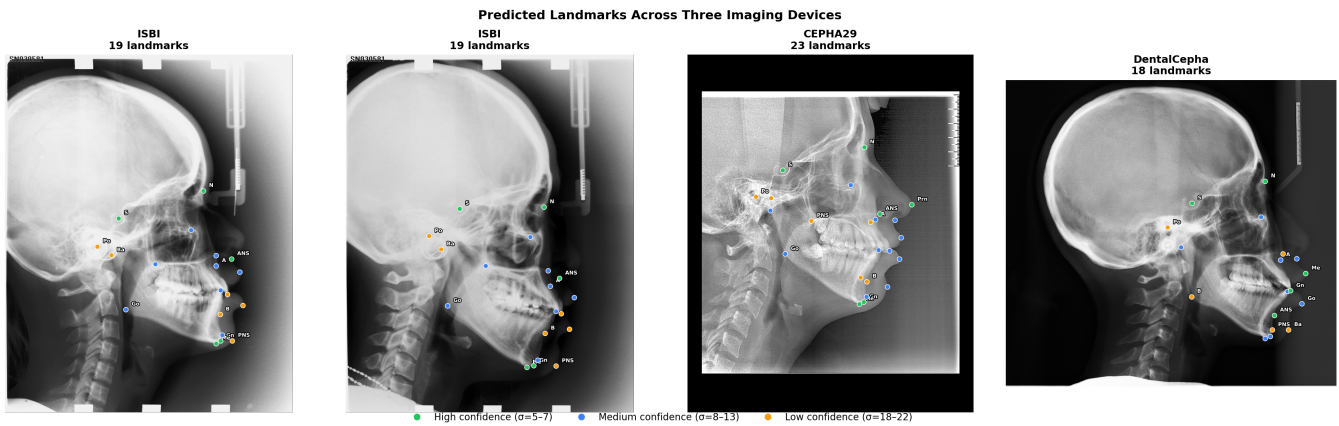


Figure 7: Predicted landmarks on four representative cephalograms spanning three imaging devices. Colors indicate confidence tier: green (high,  $\sigma=5-7$ ), blue (medium,  $\sigma=8-13$ ), orange (low,  $\sigma=18-22$ ). Key landmarks are labeled. The system produces anatomically plausible placement across diverse scanner technologies.

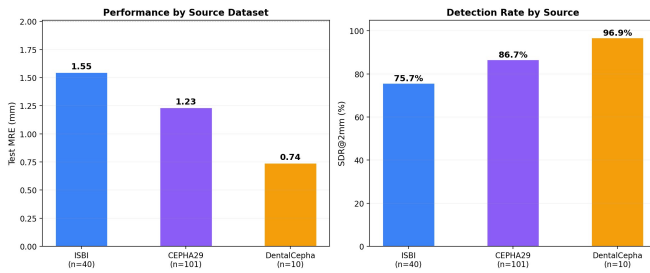


Figure 8: Cross-dataset generalization. Performance is consistent across 3 sources spanning 7+ imaging devices, confirming the anatomy-guided priors generalize across scanner technologies.

## 6.5 Limitations

Phase C contour models achieve modest Dice (0.37–0.54) using bootstrap training data; Phase D results reported here validate the geometric pipeline on clean (ground-truth) contours. SAM-assisted contour annotation would close this gap. Our 1,502-image dataset, while spanning 7+ devices, remains modest compared to general vision benchmarks. Landmarks with fewer than 50 test samples (Basion, Pm) have high metric variance.

## 7 Conclusion

We presented a system that translates the structured clinical workflow of cephalometric tracing into a computational pipeline, producing anatomy-guided spatial priors that reduce landmark detection error by 46.2% and nearly eliminate the generalization gap between validation and test performance. Three findings have implications beyond cephalometry.

First, the three-way ablation establishes a causal hierarchy: all three models (no priors, random priors, anatomical priors) converge to the same validation error, but their test-set generalization diverges dramatically (1.94, 2.24, and 1.04 mm re-

spectively). Random priors—which provide the same channel count and  $\sigma$  distributions but incorrect positions—produce *worse* generalization than no priors at all. This proves the improvement derives from anatomically correct spatial information, not from architectural capacity or generic regularization.

Second, the differential benefit pattern—soft tissue landmarks improving most, ambiguous bony landmarks next, high-contrast landmarks least—demonstrates that clinical domain knowledge is most valuable precisely where end-to-end learning fails, suggesting a general principle for medical image analysis.

Third, the topology-based extraction rules demonstrate that clinical textbook definitions (“Sella is the midpoint of the pituitary fossa”) can be translated into orientation-invariant computational geometry, opening a pathway for any domain where expert knowledge is codified but not yet computationalized.

The system achieves 1.04 mm MRE on 25 landmarks, with twelve sub-millimeter—approaching and in several cases surpassing expert observer variability. It has operated in production since April 2026 with zero inference failures.

*Patent notice: U.S. Provisional Application No. 64/039,042 and related applications.*

## References

- [1] H. W. Fields, B. E. Larson, D. M. Sarver, W. R. Proffit. *Contemporary Orthodontics*, 7th ed. Elsevier, 2024.
- [2] C.-W. Wang et al. Evaluation and comparison of anatomical landmark detection methods for cephalometric x-ray images: A grand challenge. *IEEE Trans. Med. Imaging*, 34(9):1890–1900, 2015.
- [3] C. Lindner and T. F. Cootes. Fully automatic cephalometric evaluation using random forest regression-voting. In *Proc. IEEE ISBI*, 2015.
- [4] M. Zeng et al. Cascaded convolutional networks for automatic cephalometric landmark detection. *Medical Image Analysis*, 68:101904, 2021.

- [5] R. Chen et al. Cephalometric landmark detection by attentive feature pyramid fusion and regression-voting. In *Proc. MICCAI*, pp. 873–881, 2019.
- [6] A. Jaheen et al. CephRes-MHNet: A multi-head residual network for cephalometric landmark detection. *arXiv:2511.10173*, 2025.
- [7] M. A. Khalid et al. CEPHA29: Automatic cephalometric landmark detection challenge 2023. *arXiv:2212.04808*, 2022.
- [8] H. J. Kwon et al. Automated cephalometric landmark detection with confidence regions using Bayesian CNNs. *BMC Oral Health*, 20:270, 2020.
- [9] I. Son et al. Ceph-Net: Automatic detection of cephalometric landmarks using an attention-based stacked regression network. *BMC Oral Health*, 2023.
- [10] Z. Zhong et al. An attention-guided deep regression model for landmark detection in cephalograms. In *Proc. MICCAI*, pp. 540–548, 2019.
- [11] K. Oh et al. Deep anatomical context feature learning for cephalometric landmark detection. *IEEE J. Biomed. Health Inform.*, 2021.
- [12] M. A. Khalid et al. A two-stage regression framework for automated cephalometric landmark detection. *Expert Syst. Appl.*, 124840, 2024.
- [13] M. A. Khalid et al. A benchmark dataset for automatic cephalometric landmark detection. *Scientific Data*, 2025.